ARCHIVES OF MECHANICS
Arch. Mech. **75** (6), 695–727, 2023, DOI: 10.24423/aom.4312

Static instability of an inverted plate in channel flow: state-space representation and solution approximation

P. LI*), D. ZHANG, J. CUI, H. YIN, Y. YANG

School of Mechanics and Aerospace Engineering, Southwest Jiaotong University, Chengdu, 610031, P.R. China,
e-mail): lp_vib@126.com, meiyongyuandeze@163.com (corresponding author)*

Plate-like structures in channel flow are commonly found in engineering. This paper reports a theoretical study on the static aeroelastic instability of an inverted cantilevered plate in an inviscid channel flow through the state space. This study begins with the kernel function of the flow potential determined in the Fourier domain with the help of the mirror image method. Then, the instability equation is derived from the operator theory and transformed in the state space. Finally, with Glauert's expansion, model functions, and error functions, the instability problem of such a plate has been modeled as a mathematical function approximation problem and solved by the least squares method. The derived instability equation is considered at the continuum level of description, and no approximation appears at the first equation level. The convergence and reliability of the proposed modeling and its solutions approximation are entirely tested, and it can successfully predict the instability boundary, behavior, and the channel effect. Numerical results show that the decreased channel height and asymmetric plate placement in the channel significantly decrease the critical flow velocity. The plate instability modes are close to the plate's first natural ones and not sensitive to the channel parameters. This conclusion allows further theoretical exploration of a semi-analytical approximation of the instability boundary from the obtained instability equation. The current modeling strategy in a continuum sense may provide a new idea and essential reference for other instability problems.

Key words: inverted cantilevered plate, static aeroelastic instability, channel flow, state-space representation, Glauert's series, the least squares method.

1. Introduction

The instability of flexible plates vibrating in airflow is an aeroelastic problem that has received widespread attention due to its relevance in many applications. Such a problem fundamentally involves flow and structure mechanics and has become a classical Applied Mechanics problem [1]. Wide applications have motivated various plate-interacting-with-flow models [1, 2], such as for the aircraft and missile skins [3, 4], high-speed train panels [5–9], nuclear plate assemblies [10, 11], paper making [12, 13], energy harvesters [14, 15], flow control de-

vices [17], aircraft control [18], the in-flight or swimming motion of animals [19], flapping of flags [20], and the snoring in humans [21], ranging from the dynamics of plate-type engineer structures to exploring trivial everyday phenomena.

The instability of plates in fluids has been extensively studied. As for instability analysis, linear modeling is of interest not only due to its prevalence but also to its superior understanding of the essential nature of such instability problems [1, 2]. At this time, the system can be studied by restricting to two-dimensional aeroelastic plate models, as observed in most experiments [1, 12, 13]. The plate is considered one-dimensional and beam-like; however, different theoretical models and methods can calculate the fluid force. In [17, 22], the fluid force of the plate with an infinite wall was obtained by using the series expansion in plate modes. Kornecki *et al.* [23] and Huang [21] applied the unsteady Theodorsen's theory for the fluid force to study the flutter instability of plates. Li *et al.* [5, 6] and Guo and Païdoussis [10] modeled the flow force by a time-dependent source on the plate and considered the plate as a lifting line. Li *et al.* [7, 8] and Breuker *et al.* [18] obtained the fluid force from the two-dimensional wing theory based on Glauret's expansion. Eloy *et al.* [24] used the Fourier transform for fluid force from the linear potential equation. The fluid models mentioned above mainly developed from the airfoil theory, and the plate has been modeled as a lifting surface. However, results show that imposing Kutta's condition at the plate leading edge plays a vital role in admitting a unique and accurate solution of the pressure, intrinsically because it provides an additional boundary condition when solving the Laplace equation of the fluid instead of on an open domain [24]. A continuous partial differential equation describes the original aeroelastic plate models in the above studies. The discretization methods need to be introduced for a series of ordinary differential equations, i.e., obtaining an approximated system of the original one. According to the eigenvalues or time-response information of such an approximated system, we can further determine the stability of the original system.

In addition to theoretical analysis of the fluid force based on potential flow theory, numerical solutions have also been widely applied. The discrete modeling strategy allows us obtain the ordinary differential equations directly and then analyze the eigenvalue or the time response to determine the stability. Two-dimensional numerical vortex lattice methods for plate flutter were respectively developed by Tang and Dowell [15] and Chen *et al.* [16], and a numerical panel method by Howell and Lucey [25]. A fluid-structure direct simulation based on the Navier–Stokes solver for the fluid force was developed by Watanabe *et al.* [12, 13] and Connell and Yue [26]. Using the immersed boundary method, Zhu and Peskin [27] and Huang *et al.* [28] studied the dynamics of a flutter plate. As with theoretical analysis, numerical application of Kutta's condition is also necessary to ensure the correctness of computational results.

Thanks to the development of these theories and numerical calculation methods, many important problems in flexible thin plate aeroelasticity have corresponding explanations and conclusions. The most important is the type of instability and the prediction of critical state in terms of fluid and structural parameters. Related studies show that the plate could experience two types of instability, i.e., dynamical (flutter) and static (divergence) instability. The type of instability is closely dependent on both the plate boundary conditions and flow speed. For instance, a plate with both ends simply-supported (pinned) or clamped undergoes divergence in low-speed flow [22, 23] but flutter instability in supersonic flow [1, 3, 4]. However, if this plate is cantilevered at one end and free at the other, it will flutter in low-speed flow [21] but experience divergence in supersonic flow [1, 3, 4].

In various plate-interacting-with-flow models, the plate model with one edge free and another clamped has attracted more and more interest. It is a conventional cantilevered plate when the plate can move freely on the trailing edge. When the plate moves freely at the leading edge, i.e., the flow impinges it on its free edge, it is called an inverted cantilevered plate. Our initial focus on this plate model is mainly due to its application in high-speed train skins. This model can be developed for studying the dynamical behavior of train skins with boundary relaxation loaded by a low-speed airflow (the Mach number M_{a} is about less than 0.2 for the current running speed of trains, and the airflow can be assumed incompressible). Generally, in manufacturing a high-speed train body, as shown in Fig. 1(a), many pieces of skin are bolted onto the keel of trains, and these panel-like structures can be ideally modeled as a perfect plate model with both edges clamped. However, when these panels experience long-term vibration, the bolted points between the panels and train keel start to back off, and imperfect boundary constraints appear [6–9]. An extremely dangerous case may occur if all bolted points at a panel edge completely lose efficacy. At this time, this panel naturally exhibits a geometry with an inverted configuration, as shown in Fig. 1(b). Understanding the flow-induced instability characteristics of these train skin panels, especially predicting the critical flow speed in some dangerous potential cases, is vital for their design. It is an important reason we mainly focus on the instability analysis in this study. In addition, based on this plate model, ZHANG *et al.* [29] developed a model for the instability problem of high-speed trains' panels with extremely dangerous boundary relaxation when the trains pass each other or run through tunnels, i.e., the plate is driven by a bounded flow. Their study uses a rigid wall parallel to an inverted plate to simulate the bounded flow, i.e., the ground effect. Such an effect on plate instability has been numerically and experimentally investigated. It is seen that the plate loses its stability by divergence at a lower speed, and the critical speed is quite sensitive to the distance between the plate and wall.

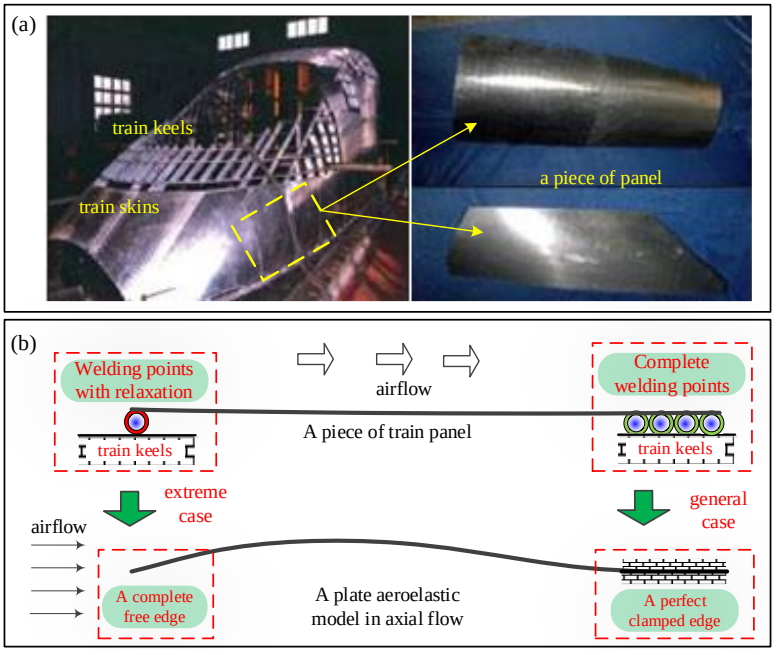

Fig. 1. Schematic diagrams of (a) the physical model of panels in high-speed trains and (b) the simplified aeroelastic (mechanical) model of an inverted cantilevered plate subjected to an axial low-speed airflow.

Meanwhile, the inverted cantilevered plate model also has other practical applications, ranging from engineering structures to exploring natural phenomena. In [30], an inverted plate-type sheet has been used to add an inserter into the channel flow. It is shown that such an inverted configuration can more effectively disturb the flow and promote turbulence to improve the heat transfer performance of the air-cooled systems, which are widely used in the radiators of buildings and trains. In addition to these typical engineering applications, this type of inverted plate model has been applied to study the flapping motion of leaves in trees affected by wind. Because the wind may blow in any direction, some leaves may hold in an inverted orientation to the wind [31]. This study sheds new light on how plants reconfigure their shapes and orientations to reduce drag and damage in strong winds. In [32], the inverted plate is used for studying the clapping motion of a book under aerodynamic loading, and it can reveal the book pages' accumulation and collapse.

Another engineering application worthy of special attention is that the inverted cantilevered plate model has been newly put forward as an energy harvester. It provides an essential supplement to the traditional studies relying on the conventional cantilevered plate models. The energy harvester design based

on a cantilevered plate model has been widely studied due to its oscillation with growing amplitude after it undergoes instability in a low-speed axial flow [33]. However, under the previously studied conditions, this kind of harvester generally has a high working flow speed because of the flag-type plate orientation, limiting its wide applications. In order to make such types of harvesters work at lower flow speed, some emphasis has been placed on studying the effect of plate orientation on critical velocity. The inverted configuration of a cantilevered plate has drawn extensive attention from researchers. An inverted plate configuration design is a dynamical analog to an inverted pendulum under gravitational force. It is shown that, under compression, such a pendulum is generally more susceptible to instability than its counterpart with reverse end conditions [34]. In addition to the feature of lower critical velocity, new equilibrium states generally accompany static instability and bifurcations, and it is very beneficial to the design of energy harvesters [35]. The instability and post-instability behaviors of the inverted plate ensure excellent potential applications for harvesting flow energy.

Although an inverted plate generally has the above potential application characteristics compared with the conventional ones, the essential controllability of the critical speed, which is an actual performance for the energy harvesters, can not be achieved only by changing the orientation of a plate. Thus, some effective measures to improve the coupling effect between fluid and structure are proposed and studied. Placing a bluff body ahead of the plate and using the bluff body's wake effect to decrease the critical flow speed is successfully realized in [36]. The plate could undergo large amplitude oscillations at relatively low flow speed. MAZHARMANESH *et al.* [37] suggest a two-parallel-plates model and investigates the coupled fluid-structure-electric dynamics of these two plates in tandem, side-by-side, and staggered arrangements. It is shown that the critical speed significantly decreases due to the increasing coupling effect of these two plates. Similar results of the effect of bounded flow on the plate instability have also been reported in the authors' study [29]. This study indicates that when an inverted plate is used as an energy harvester, using the ground effect to regulate the plate's critical flow speed is an effective and promising direction of research.

The instability behaviors of the inverted plates have been widely studied due to their importance in engineering and nature. These studies, encompassing theoretical, numerical, and experimental approaches, focus on understanding the mechanisms underlying this instability. In line with traditional research, the plate is considered to be one-dimensional. Furthermore, the fluid force is generally solved using the classic aerodynamic theory of lift line or surface, such as Polhamus leading-edge suction analogy [35], Theodorsen's theory [38, 39], and the Possio integral equation [40]. In parallel to the theoretical analysis,

the experiments [41] and numerical studies, such as using the vortex panel method [29], the coupled fluid-structure solver based on fully coupled Navier–Stokes and nonlinear structural dynamic equations [42, 43], immersed boundary method [44, 45], immersed boundary-lattice Boltzmann method [46, 47], also provide a great supplement to the theoretical analysis. It is shown that the inverted flag-type plate has a richness of instability and post-instability behaviors. Such a plate may remain straight or flutter slightly for a small flow speed; with the flow speed increasing, the plate flips from side to side [41]. Its deflection is periodic, and flutter occurs, but if the flow speed continues to grow, the plate will bend in one direction and maintain a highly curved shape with slight fluttering [41]. An extended study of [41] is completed by Sader *et al.* [39], and they conducted a set of experiments to further sketchily mark the boundaries between different plate states in terms of the aspect ratio. It is worth noting that because flows in engineering generally have large Reynolds numbers, apart form the eddy viscosity to account for turbulence, the fluid can basically be assumed to be inviscid. Then, the potential flow theory is often used for the theoretical analysis of inverted plates [35, 38]. Theoretical results show that the inverted plate exhibits vibrant nonlinear static responses if its geometrical nonlinearity is considered. The plate system would experience both the sub-critical and supercritical pitchfork bifurcations with varying aspect ratios. On the other hand, it is well known that the complex nonlinear motion of the plate after instability is related to nonlinearity, but more importantly, it is related to the type of instability experienced, and the appearance of new equilibrium states is closely associated with static instability [35, 38, 41]. This conclusion is also a vital motivation for this paper, paying particular attention to the static instability of an inverted plate. The studies mentioned above provide rich references in modeling and analyzing the instability problem of the inverted plate.

However, we have noticed a problem in reviewing the modeling strategy of the previous studies. It is known that in these studies, the original aeroelastic plate system was discretized, and the equations that were finally solved were the discretized ones. In the above studies of plate instability, the critical speed was mainly determined according to the characteristics of eigenvalues or the time responses. However, these crucial data do not come from the original system. The approximated system is generally obtained with necessary assumptions and approximations, such as using the Galerkin method [1, 5, 6, 19, 22, 23] or the finite difference method [25, 26, 29] to transform the partial differential equations into ordinary ones. Approximation appears at the first level for deriving the instability equation rather than the solutions at the end level. The approximation introduced at the equation level may limit the generality of the original system and is not conducive to revealing some important internal laws because there is no immediate solution to the original system. Of course, the approximate equa-

tion is generally accepted when it can provide a good enough approximation of the exact solution; however, this can be misleading when the original continuum equations have more than one solution or no solutions at all. A good view of such problems in aero-elasticity modeling is detailed and discussed by BALAKRISHNAN [48] in his book. Most importantly, his study provides a valuable modeling strategy in the framework of the continuum theory for aeroelasticity problems. One study of particular relevance to the instability analysis methodology of the present study is the authors' recent work in [9]. In this study, the authors carried out a static instability analysis in a continuum sense for a plate in airflow and with any number of cracks. Because of discontinuity caused by cracks, the author introduced the operator theory to derive the analytical plate instability equation and then accessed the numerical solutions. This work provides an essential reference and inspiration for our present study.

This paper gains its motivation from [29] and aims to extend this study from the unilateral to bilateral wall effect, i.e., placing the plate into a channel, see Fig. 2. The primary purpose of the present study is to explore the channel effect on the static instability of the inverted plate in an axial airflow. As shown in Fig. 2, in the present model, the channel height (H) and the distance between the plate and bottom wall (d) are the two variable parameters that may provide more diverse variations of the critical flow speed. In addition to the model improvements, we designed to address the present problem, the aeroelastic instability of an inverted cantilevered plate in a channel flow within a framework in a continuum sense; this is another essential purpose of this paper. As the present model can degenerate into that of [29], this paper is expected to provide different analytical perspectives and necessary supplements to the previous study.

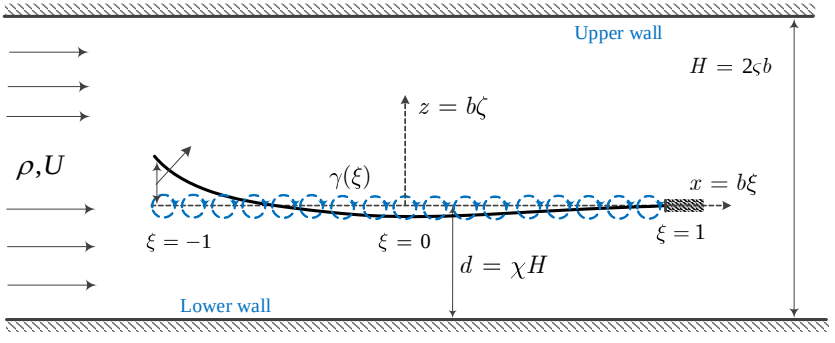

FIG. 2. Schematic of an inverted cantilevered plate in a channel airflow.

As inspired by [9, 48], the main modeling idea of the present instability problem in this paper is to approximate the solution of the instability equation in

a continuum sense rather than the classical discrete method. In this work, as shown below, we do not bring approximation in the derivation of the instability equation and approximation as needed only at the end-level calculation of the solution to the instability equation. The structure and content of this paper are organized as follows. We begin in Section 2 with the model and equation of the plate aero-elastic instability problem. We first analytically determine the kernel function of the flow potential in the Fourier domain with the help of the mirror image method and then complete the derivation of the instability equation of the present problem in the state-space formulation. It has been represented as a mathematical function approximation problem with the critical flow speed and instability modes as the objective functions. With this equation, Section 3 gives its approximated solution using the least squares method with the help of polynomial expansion and Glauert's expansion. Then, based on the numerical results, Section 4 presents a comprehensive analysis of the effect of the wall confinement on the plate insatiability behaviors. Finally, some general conclusions of this study and open problems are summarized in Section 5.

2. Theoretical modeling procedure

2.1. Problem description and basic equations

This study examines a two-dimensional aeroelastic problem in which a thin, flexible plate with the length $L = 2b$ and thickness h, is placed inside a channel flow, as shown in Fig. 2. The plate is clamped at its trailing edge and free at the leading one, which is different from the conventional one with a free trailing edge. The plate is set at a distance d from the lower rigid wall of a channel with height H. The plate bending rigidity is $D = Eh^3/12(1-\upsilon^2)$, where E and υ are the Young modulus and the Poisson ratio of the plate, respectively. The incoming flow is low subsonic and assumed potential, and the inflow direction is parallel to the x-direction. The density and inflow speed of the flow are ρ and U, respectively. Furthermore, the plate deflection w defined from the rest is assumed in the same order as the plate thickness. The equations of this problem are derived in non-dimensional form using the following non-dimensional parameters

$$\eta = \frac{w}{b}, \quad \xi = \frac{x}{b}, \quad \zeta = \frac{z}{b}, \quad \lambda = \frac{\rho U^2 L^3}{D}, \quad \varsigma = \frac{H}{L}, \quad \chi = \frac{d}{H}, \tag{2.1}$$

where λ is the non-dimensional dynamic pressure; ς is the channel confinement ratio and χ is the plate placement ratio, and they are the characteristic parameters of the channel about its effect.

For the static divergence instability concerned in this paper, the plate is assumed beam-like, and its motion equation can be expressed as the linear static

Euler–Bernoulli beam equation with corresponding boundary conditions given on both edges; thus

$$\eta^{(4)} = -p(\xi), \tag{2.2a}$$

$$\eta^{(2)}(\xi = -1) = \eta^{(3)}(\xi = -1) = 0, \tag{2.2b}$$

$$\eta(\xi = 1) = \eta^{(1)}(\xi = 1) = 0, \tag{2.2c}$$

where $(\cdot)^{(n)}$ is n-th order ordinary differential operator in respect to ξ. The pressure difference between the upper and lower surfaces of the plate (i.e., the pressure across the plate) is defined as

$$p(\xi) = p_{0^+}(\xi) - p_{0^-}(\xi). \tag{2.3}$$

As the flow is assumed inviscid and potential, the pressure on plate surfaces can be calculated from the Bernoulli equation; thus

$$p_{0^\pm}(\xi) = -\frac{\lambda}{8}\partial_\xi \varphi(\xi, \zeta = 0^\pm), \tag{2.4}$$

where $\varphi(\xi, \zeta)$ is the non-dimensional flow potential function that should satisfy the governing equation

$$\partial_\xi^2 \varphi + \partial_\zeta^2 \varphi = 0, \tag{2.5}$$

and also the following boundary conditions

$$\partial_\zeta \varphi|_{\zeta=0} = 0, \quad \xi \notin [-1, 1], \tag{2.6a}$$

$$\partial_\zeta \varphi|_{\zeta=-2\varsigma\chi} = 0, \quad \xi \in (-\infty, \infty), \tag{2.6b}$$

$$\partial_\zeta \varphi|_{\zeta=2\varsigma(1-\chi)} = 0, \quad \xi \in (-\infty, \infty), \tag{2.6c}$$

$$\partial_\zeta \varphi|_{\zeta=0^\pm} = v_I^\pm = \theta(\xi), \quad \xi \in [-1, 1], \tag{2.6d}$$

$$p = 0, \quad \xi \notin [-1, 1], \tag{2.6e}$$

$$\lim_{\xi \to 1} p = 0. \tag{2.6f}$$

In addition, the potential function and the pressure also need to satisfy the following far-field conditions [40]

$$\partial_\xi \varphi|_{\xi^2+\zeta^2 \to \infty} = 0, \tag{2.7a}$$

$$\partial_\zeta \varphi|_{\xi^2+\zeta^2 \to \infty} = 0, \tag{2.7b}$$

$$p|_{\xi^2+\zeta^2 \to \infty} = 0. \tag{2.7c}$$

These two Eqs. (2.6b-c) imply that the flow has no normal speed on the top and bottom walls. In Eq. (2.6d), $\theta(\xi)$ is the plate slope $\theta(\xi)$ is defined as

$$\theta(\xi) = \eta^{(1)}(\xi),$$

and $v_I^{\pm}$ are the down-wash flow velocities on the plate surfaces. Obviously, it is seen that there should be the same down-wash velocity on both surfaces of the plate; that is

$$v_I^+ = v_I^- = v_I(\zeta = 0^{\pm}), \tag{2.8}$$

and it is also called as the continuity condition of flow velocity.

The plate is assumed to experience slight deflection for the static instability problem we studied here. Then, it can be modeled as a lifting problem of a thin airfoil with zero-thickness at a slight angle of attack. As inspired by [11], the solution based on vortex distribution is used because of its straightforward derivation and physical description. As shown in Fig. 2, the present static problem is modeled by a continuous and time-independent vortex distribution of $\gamma(\xi)$ placed on the ξ-axis. And the boundary condition should also be fulfilled on this axis through the Biot–Savart kernel; that is

$$\theta(\xi) = -\frac{1}{2\pi}\int_{-1}^{1} \gamma(\xi')\mathcal{K}(\xi,\xi')\,d\xi', \tag{2.9}$$

where $\mathcal{K}(\xi,\xi')$ is the unknown kernel function for the linearized problem satisfying the non-penetration boundary conditions on the top and bottom walls. It should be emphasized that the inverted plate studied in this paper undergoes static instability [35, 39, 40] and the effects of the tail-vortex can be neglected [39, 40]. So, the above equation does not include the effect of the wake. However, for the dynamical instability problem of plate fluttering, such an effect of vorticity shedding into flow wake is time-dependent and should be carefully evaluated [7, 8, 23, 24].

The above equation indicates that the vortex distribution $\gamma(\xi)$ should be determined as a function of the continuous plate slope function of $\theta(\xi)$. Then, γ is a functional of θ and its domain of definition is ξ; thus

$$\gamma(\xi) = \gamma[\theta](\xi).$$

Once the vortex distribution $\gamma[\theta](\xi)$ is obtained, the potential on the plate surfaces can be calculated from the following integration with assuming the zero-value of potential at the plate leading edge; that is

$$\varphi(\xi,\zeta = 0^{\pm}) = \pm\frac{1}{2}\int_{-1}^{\xi} \gamma[\theta](\xi)\,d\xi. \tag{2.10}$$

Then the pressure difference across the plate is calculated as

$$p(\xi) = -\frac{\lambda}{8}\gamma[\theta](\xi). \tag{2.11}$$

Substituting $\gamma[\theta](\xi)$ into Eq. (2.11), the condition of Eq. (2.6f) becomes

$$\gamma[\theta](\xi = 1) = 0, \tag{2.12}$$

that is a condition requiring that the airflow leaves the plate trailing edge smoothly and the flow velocity there be finite. It is Kutta's condition in terms of γ applied in the present modeling.

2.2. Derivation of the kernel function

Equation (2.5) is a partial differential equation, to obtain its solution, we begin to solve it in the frequency domain. The following derivation starts with applying the Fourier transform ($\mathcal{F}[\cdot]$) in the ξ variable to both sides of Eq. (2.5) to obtain

$$\partial_\zeta^2 \hat{\varphi} = \omega^2 \hat{\varphi}, \tag{2.13}$$

where $\hat{\varphi} = \int_{-\infty}^{+\infty} \varphi e^{i\omega\xi}\, d\xi$, $i^2 = -1$.

The above equation implies the basic solutions of exponential form. For the case of the plate placed in an unbounded flow, [40] gives its solution as follows

$$\hat{\varphi}(\omega, \zeta) = \begin{cases} \hat{\varphi}^+ e^{-|\omega|\zeta} & (\zeta > 0), \\ \hat{\varphi}^- e^{+|\omega|\zeta} & (\zeta < 0), \end{cases}$$

where $\hat{\varphi}^\pm = \hat{\varphi}(\zeta = 0^\pm)$ are the potentials on these two plate surfaces.

However, when the flow is confined in a channel, the potential should also satisfy the flow boundary conditions on these two channel walls, i.e., Eqs. (2.6a-b). Hence, the method of images is applied in the present modeling of these two conditions. As shown in Fig. 3, a series of images of the plate and walls are added. According to the superposition principle, the flow potential of the present system is calculated as

$$\begin{aligned} &\hat{\varphi}(\omega, \zeta; \varsigma, \chi) \\ &= \hat{\varphi}^+ \left[\begin{array}{c} e^{-|\omega|\zeta} + \sum\limits_{n=1}^{\infty} e^{-|\omega|(\zeta+4n\varsigma)} + \sum\limits_{n=0}^{\infty} e^{|\omega|(\zeta-4n\varsigma-4\varsigma+4\chi\varsigma)} \\ - \sum\limits_{n=1}^{\infty} e^{|\omega|(\zeta-4n\varsigma)} - \sum\limits_{n=0}^{\infty} e^{-|\omega|(\zeta+4n\varsigma+4\chi\varsigma)} \end{array} \right], \quad (\zeta > 0), \end{aligned} \tag{2.14}$$

and

$$\begin{aligned} &\hat{\varphi}(\omega, \zeta; \varsigma, \chi) \\ &= \hat{\varphi}^- \left[\begin{array}{c} e^{|\omega|\zeta} + \sum\limits_{n=1}^{\infty} e^{|\omega|(\zeta-4n\varsigma)} + \sum\limits_{n=0}^{\infty} e^{-|\omega|(\zeta+4n\varsigma+4\chi\varsigma)} \\ - \sum\limits_{n=1}^{\infty} e^{-|\omega|(\zeta+4n\varsigma)} - \sum\limits_{n=0}^{\infty} e^{|\omega|(\zeta-4n\varsigma-4\varsigma+4\chi\varsigma)} \end{array} \right], \quad (\zeta < 0). \end{aligned} \tag{2.15}$$

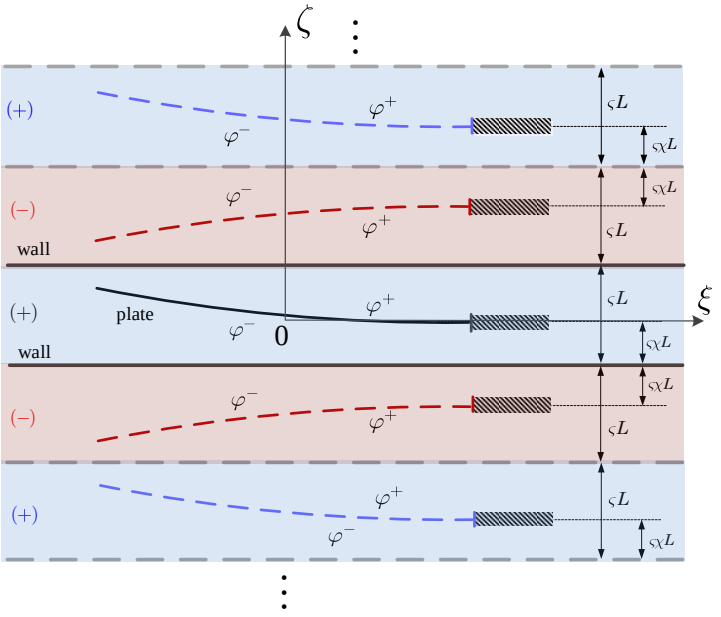

FIG. 3. The mirror image system of the plate and walls. Blue dashed lines have the same sign as the actual plate, and red dashed the opposite sign.

With the above results and using Eq. (2.6d), the down-wash velocities on the two plate surfaces are obtained as

$$\frac{\hat{v}_I^{\pm}}{|\omega|} = - \hat{\varphi}^+ \Big[1 + 2\sum_{n=1}^{\infty} e^{-|\omega|(4n\varsigma)} - \sum_{n=0}^{\infty} e^{-|\omega|(4n\varsigma+4\chi\varsigma)} - \sum_{n=0}^{\infty} e^{|\omega|(-4n\varsigma-4\varsigma+4\chi\varsigma)}\Big], \tag{2.16}$$

which implies that the important continuity condition of flow velocity listed in Eq. (2.8) has been exactly satisfied, and therefore, we apply $\hat{v}_I^{\pm} = \hat{\theta}$ in the following derivation.

Regarding the summation of each term in Eq. (2.16) as the summation of a geometric series, then these two equations can be further simplified as

$$\frac{\hat{\theta}}{|\omega|} = -\hat{\varphi}^+[1 + \Theta(\omega; \varsigma, \chi)], \tag{2.17}$$

where

$$\Theta(\omega; \varsigma, \chi) = \frac{2e^{-4|\omega|\varsigma} - e^{-4|\omega|\varsigma\chi} - e^{-4|\omega|\varsigma(1-\chi)}}{1 - e^{-4|\omega|\varsigma}},$$

is a function associated with characteristic parameters of the channel and refers to the channel effect.

According to Eq. (2.10), we obtain the relationship between the following two potentials

$$\hat{\varphi}^+ = -\hat{\varphi}^-,$$

and then the potential difference between two plate surfaces is calculated as

$$\Delta\hat{\varphi} \equiv \hat{\varphi}^+ - \hat{\varphi}^- = 2\hat{\varphi}^+. \tag{2.18}$$

For the pressure difference, a substitution of Eq. (2.18) into Eq. (2.4) yields

$$\hat{p} = -i\frac{\lambda}{8}\omega\Delta\hat{\varphi} = -i\frac{\lambda}{4}\omega\hat{\varphi}^+. \tag{2.19}$$

Finally, substituting Eq. (2.17) into Eq. (2.19) gives

$$2\hat{\theta} = -\frac{|\omega|}{i\omega}[1 + \Theta(\omega;\varsigma,\chi)]\hat{\gamma}, \tag{2.20}$$

which gives the relation between the down-wash velocity and vortex distribution, and it is a kind of the Possio equation in the Fourier domain [40, 48]. The above equation shows that the flow velocity on the plate induced by $\theta(\xi)$ is equal to the induced velocity of the vortex distribution $\gamma(\xi)$. However, it does not mean that when the plate attack angle of $\theta(\xi)$ is known, the fluid forces of the two cases also satisfy such a linear superposition rule.

Next, we need to establish the final equation by breaking Eq. (2.20) into simple multipliers [40, 48]. Note that the Hilbert transform ($\mathcal{H}[\cdot]$) of a function $f(\xi)$ has the following relation with the Fourier transform, i.e.,

$$\mathcal{F}[\mathcal{H}[f(\xi)]] = \frac{|\omega|}{i\omega}\mathcal{F}[f(\xi)],$$

and in view of Eq. (2.6a) we correspondingly define the following projection operator

$$\mathcal{P} : L^p(-\infty,\infty) \to L^p[-1,1].$$

Then using the above mentioned operators and applying the inverse transformation to both sides of Eq. (2.20) results in

$$\theta(\xi) = -\frac{1}{2\pi}\int_{-1}^{1}\gamma(\xi')\left[\frac{1}{\xi-\xi'} + \int_{-\infty}^{+\infty}\frac{\mathcal{T}(s-\xi';\varsigma,\chi)}{\xi-\xi'}\,ds\right]d\xi', \tag{2.21}$$

and the function $\mathcal{T}(s;\varsigma,\chi)$ is defined as

$$\mathcal{T}(s;\varsigma,\chi) = \frac{1}{2\pi}\int_{-\infty}^{+\infty}\Theta(\omega;\varsigma,\chi)\cos(\omega s)\,d\omega. \tag{2.22}$$

A comparison of the above equation with Eq. (2.9) clearly gives that

$$\mathcal{K}(\xi,\xi';\varsigma,\chi)=\frac{1}{\xi-\xi'}\left[1+\int_{-\infty}^{+\infty}\mathcal{T}(s-\xi';\varsigma,\chi)\,ds\right]. \tag{2.23}$$

It is obvious that the first term in this kernel function is related to the case of an unbounded flow, and the second term refers to the channel effect.

Although we have obtained the expression of the kernel function $\mathcal{K}(\xi,\xi';\varsigma,\chi)$, it is still incredibly challenging to solve the function $\mathcal{T}(s;\varsigma,\chi)$ analytically. Therefore, numerical integration is applied for both $\mathcal{T}(s;\varsigma,\chi)$ and $\mathcal{K}(r;\varsigma,\chi)$. In Fig. 4, we plot its numerical results. It is seen that $\mathcal{T}(s;\varsigma,\chi)$ decreases with the increase of $|s|$ and reaches its maximum value when $s=0$. The peak value of $\mathcal{T}(s;\varsigma,\chi)$

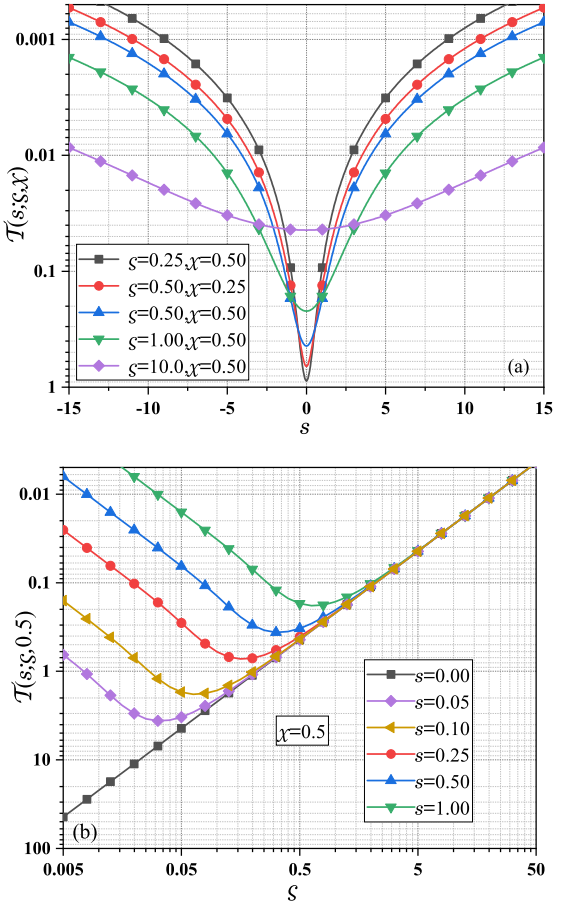

Fig. 4. Numerical evaluation of function $\mathcal{T}(s;\varsigma,\chi)$.

decreases as ς is increasing. With the increase of ς, i.e., the wall confinement decreases, the decay rate of these functions becomes smaller and approaches zero. As shown in Fig. 4(b), when ς is large enough, $\mathcal{T}(s;\varsigma,\chi)$ is approaching zero in any finite region close to zero, which implies that the term in Eq. (2.22) is also approaching zero and that the wall effect is negligible. At this time, the problem becomes the case of an unbounded flow, i.e., without the channel effect.

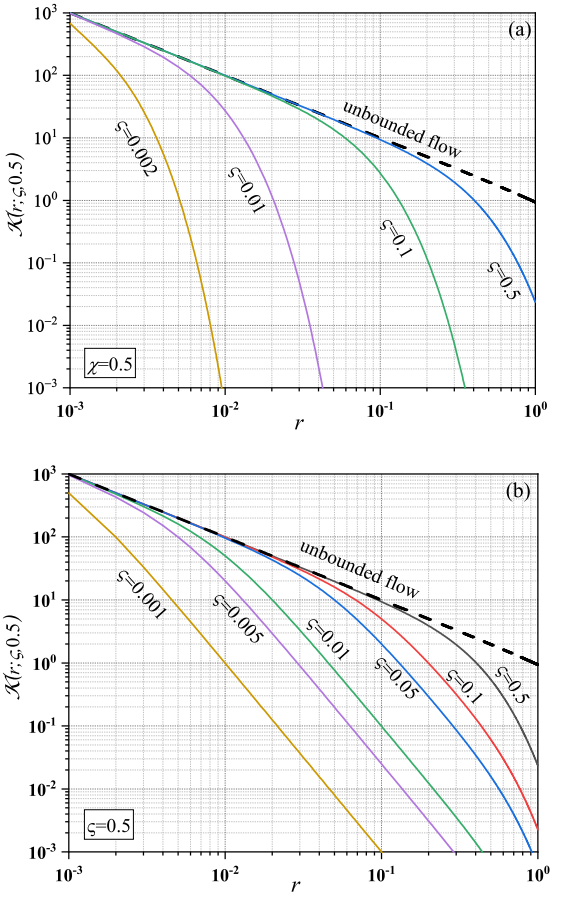

FIG. 5. Numerical evaluation of the kernel function $\mathcal{K}(r;\varsigma,\chi)$.

The dependence of the kernel function $\mathcal{K}(r;\varsigma,\chi)$ on $r=\xi-\xi'$ for various ς and χ is shown in Fig. 5. It appears that the decrease of either ς and χ leads to a rapid increase of $\mathcal{K}(r;\varsigma,\chi)$, implying that it is mostly affected by the near-field vortices of the plate. In addition, the kernel function approaches the case of unbounded flow as the ς or χ increases.

2.3. Instability equation representation in state space

In order to obtain the analytical equation of the instability problem, as motivated and inspired by work in [9, 48], we rewrite Eq. (2.2a) in the following state-space formulation, and it becomes [40]

$$\mathrm{d}\mathcal{W} = \mathbf{B}\mathcal{W} + \mathcal{B}\mathcal{W}, \tag{2.24}$$

where

$$\mathbf{B} = \begin{pmatrix} 0 & 1 & 0 & 0 \\ 0 & 0 & 1 & 0 \\ 0 & 0 & 0 & 1 \\ 0 & 0 & 0 & 0 \end{pmatrix}, \quad \mathcal{B} = \begin{pmatrix} 0 & 0 & 0 & 0 \\ 0 & 0 & 0 & 0 \\ 0 & 0 & 0 & 0 \\ 0 & -p[\cdot] & 0 & 0 \end{pmatrix}, \quad \mathcal{W} = \begin{pmatrix} \eta \\ \theta \\ \partial_\xi \theta \\ \partial_\xi^2 \theta \end{pmatrix}.$$

According to [40], the solution of Eq. (2.24) is obtained by the variation of parameters formula as

$$\mathcal{W}(\xi) = \mathcal{W}(-1)e^{\mathbf{B}(\xi+1)} + \int_{-1}^{\xi} e^{\mathbf{B}(\xi-s)}\mathcal{B}\mathcal{W}(s)\,ds, \tag{2.25}$$

where

$$e^{\mathbf{B}s} = \begin{pmatrix} 1 & s & \frac{s^2}{2} & \frac{s^3}{6} \\ 0 & 1 & s & \frac{s^2}{2} \\ 0 & 0 & 1 & s \\ 0 & 0 & 0 & 1 \end{pmatrix}.$$

Next, a rearrangement on both sides of Eq. (2.25) gives

$$\mathcal{D}\mathcal{W}(\xi) = e^{\mathbf{B}(\xi+1)}\mathcal{W}(-1), \tag{2.26}$$

where

$$\mathcal{D} = \begin{pmatrix} \mathcal{I}[\cdot] & -\mathcal{R}_1[\cdot] & 0 & 0 \\ 0 & (\mathcal{I} - \mathcal{R}_2)[\cdot] & 0 & 0 \\ 0 & -\mathcal{R}_3[\cdot] & \mathcal{I}[\cdot] & 0 \\ 0 & -\mathcal{R}_3[\cdot] & 0 & \mathcal{I}[\cdot] \end{pmatrix},$$

$$\mathcal{R}_n[\cdot](\xi) = \frac{\lambda}{8}\int_{-1}^{\xi} \frac{(\xi - s)^{4-n}}{(4-n)!}\gamma[\cdot](s)\,ds, \tag{2.27}$$

and $\mathcal{I}[\cdot]$ is the identity operator.

Applying the inverse operator of $\mathcal{D}$ to both sides of Eq. (2.26) yields

$$\mathcal{W}(\xi) = \mathcal{D}^{-1} e^{\mathbf{B}(\xi+1)} \mathcal{W}(-1), \tag{2.28}$$

where

$$\mathcal{D}^{-1} = \begin{pmatrix} \mathcal{I}[\cdot] & \mathcal{R}_1(\mathcal{I}-R_2)^{-1}[\cdot] & 0 & 0 \\ 0 & (\mathcal{I}-R_2)^{-1}[\cdot] & 0 & 0 \\ 0 & \mathcal{R}_3(\mathcal{I}-R_2)^{-1}[\cdot] & \mathcal{I}[\cdot] & 0 \\ 0 & \mathcal{R}_4(\mathcal{I}-R_2)^{-1}[\cdot] & 0 & \mathcal{I}[\cdot] \end{pmatrix}.$$

Now considering the boundary conditions of Eq. (2.2b) in the above equation yields the deformation inside the plate in terms of its values at the leading edge; thus

$$\begin{pmatrix} \eta \\ \theta \end{pmatrix}_{\xi} = \mathcal{C}(\xi) \begin{pmatrix} \eta \\ \theta \end{pmatrix}_{\xi=-1}, \tag{2.29}$$

where

$$\mathcal{C}(\xi) = \mathbf{E}[\mathcal{D}^{-1}\ e^{\mathbf{B}(\xi+1)}]\mathbf{E}^{\mathrm{T}},$$
$$\mathbf{E} = [\mathbf{I}_{2\times 2}\ \mathbf{0}_{2\times 2}].$$

It is obvious that $\mathcal{C}(\xi)$ is dependent on ξ and is similar to a transfer function correcting the plate's internal deformation and its boundary.

We turn to consider another boundary condition, i.e., Eq. (2.2c) in the above equation and arrive at

$$\begin{pmatrix} \eta \\ \theta \end{pmatrix}_{\xi=1} = \mathcal{C}(1) \begin{pmatrix} \eta \\ \theta \end{pmatrix}_{\xi=-1} = \mathbf{0}, \tag{2.30}$$

and then the plate slope at the trailing edge holds

$$\theta(1) = (\mathcal{I}-\mathcal{R}_2)^{-1}[\theta(-1)](\xi) = 0. \tag{2.31}$$

Because the plate is free at the leading edge, mathematically implying that Eq. (2.30) should have a non-trivial solution and, most importantly, allows us to satisfy the following condition

$$\det[\mathcal{C}(1)] = (\mathcal{I}-\mathcal{R}_2)^{-1}[\mathcal{U}(\xi)]\big|_{\xi=1} = 0, \tag{2.32}$$

where $\mathcal{U}(\xi)$ is a function that always has the value of $\theta(-1)$ for any ξ.

As for the linear equation of Eq. (2.32), we can assume $\mathcal{U}(\xi) = c$, where c is a non-zero constant. Then, a comparison of Eqs. (2.31) and (2.32) allows us to find the critical value of the plate slope function at the leading edge; that is

$$\theta_{\mathrm{cr}}(-1; \varsigma, \chi) = c, \tag{2.33}$$

which shows that the values of the plate slope function at the leading edge are independence on the characteristic parameters of the channel. Since c is arbitrary, we can further let $c = 1.0$ in the following discussion, i.e., the instability mode of the plate slope has been normalized by its value at the leading edge.

Then substituting Eq. (2.33) into the second line of Eq. (2.29) yields the equation for the critical plate slope (i.e., the plate instability modes)

$$\theta_{\mathrm{cr}}(\xi) = (\mathcal{I} - \mathcal{R}_2)^{-1}[\mathbf{1}](\xi), \tag{2.34}$$

where the function $\mathbf{1}(\xi)$ always has value 1 for any ξ.

Applying the operator $(\mathcal{I} - \mathcal{R}_2)$ to both sides of Eq. (2.34) yields

$$(\mathcal{I} - \mathcal{R}_2)[\theta_{\mathrm{cr}}](\xi) = \mathbf{1}(\xi). \tag{2.35}$$

Finally, a substitution of Eq. (2.27) into Eq. (2.35) and considering Eq. (2.2c) allows

$$\theta_{\mathrm{cr}}(\xi) - \frac{\lambda_{\mathrm{cr}}}{16} \int_{-1}^{\xi} (\xi - s)^2 \gamma[\theta_{\mathrm{cr}}](s)\, ds = 1. \tag{2.36}$$

Since $\theta_{\mathrm{cr}}\,(\xi = 1) = 0$ at the plate clamped end, then we can obtain

$$-\frac{\lambda_{\mathrm{cr}}}{16} \int_{-1}^{1} (1 - s)^2 \gamma[\theta_{\mathrm{cr}}](s)\, ds = 1. \tag{2.37}$$

The above equations give the relationship between λ_{cr} and γ, facilitating the prediction of λ_{cr}. It is worth noting that this relationship cannot be given by traditional discrete methods, which is the purpose of this paper based on the "continuum sense".

The above equations are derived in the state space for the present plate instability problem in terms of the critical dynamic pressure $\lambda_{\mathrm{cr}}(\varsigma, \chi)$ and the instability modes $\theta_{\mathrm{cr}}(\xi; \varsigma, \chi)$ as the unknown functions to be determined. At this state, there is no approximation for its acquisition at the equation level, and this equation for instability is still on the continuum.

It is seen that solving the instability equations is equivalent to finding the objective functions of θ_{cr} and λ_{cr} precisely at the same time. Intrinsically, it is a mathematical function approximation problem. This equation theoretically characterizes the relation between the critical speed and the instability modes when the system is unstable. It can provide the possibility of revealing some inherent rules contained in the original system from its exact equation but not from the data of an approximated one.

3. Solution approximation

The above theoretical modeling works with a continuum representation of the plate instability problem and entirely differs from the traditional one, approximating the equation at the beginning. Now we turn to the end-level calculation of the solution of θ_{cr} and λ_{cr}. At the current state, we need to make some approximations in applying numerical calculations for θ_{cr} and λ_{cr} since they are difficult to be analytically determined from such an integral equation of Eq. (2.9).

This section focuses on numerically approximating the solution of Eq. (2.36). For the convenience of expression, we omit the subscript symbol of 'cr' in the following equations of this section. We begin by utilizing the series-based function and then apply the least squares method to access the approximated solution of $\theta(\xi)$ and λ.

3.1. Least squares solution of fluid

Note that $\gamma(\xi)$ and $\theta(\xi)$ are continuous functions of ξ within $[-1, 1]$, and then according to the Stone–Weierstrass theorem [9, 40], we assume that they can be respectively expressed as a combination of a series of basis functions; thus

$$\theta(\xi) = \sum_{n=1}^{N} A_n \Theta_n(\xi), \tag{3.1a}$$

$$\gamma(\xi) = \sum_{n=1}^{N} A_n \Upsilon_n(\xi), \tag{3.1b}$$

where Θ_n are the basis functions of the slope and Υ_n the vortex distribution functions for Θ_n.

According to the Stone–Weierstrass theorem, any continuous function defined on a closed interval can be uniformly approximated as closely as desired by a polynomial function. In view of Eq. (2.2c), the basis functions $\Theta_n(\xi)$ are further assumed as

$$\Theta_n = \frac{(1-\xi)^n}{2^n}, \tag{3.2}$$

which always satisfy the boundary condition at the plate clamped end, i.e., $\Theta_n(\xi = 1) = 0$.

Next the vortex distribution function when the slope is $\Theta_n(\Upsilon_n)$ should be solved. A substitution of Eq. (3.1) into Eq. (2.9) yields

$$\Theta_n(\xi) = \frac{1}{2\pi} \int_{-1}^{1} \Upsilon_n(\xi') \mathcal{K}(\xi, \xi')\, d\xi'. \tag{3.3}$$

Notice the Kutta condition of Eq. (2.12), Υ_n should be zero at $\xi = 1$. In order to obtain an expression that is complete and satisfies this condition, as inspired by [5, 7], we further expand $\Upsilon_n(\xi)$ in terms of the Glauert series using the coordinate transformation $\xi = \cos\psi$; that is

$$\Upsilon_n[\Theta_n](\xi) = \sum_{k=0}^{N_g} {}^{g}_{n}a_k(\Theta_n)\mathcal{G}_k(\psi), \tag{3.4}$$

where $\mathcal{G}_k$ are the Glauert's function and defined as

$$\mathcal{G}_k(\psi) = \begin{cases} \cot\frac{\psi}{2} & (k=0), \\ \sin k\psi & (k \neq 0). \end{cases}$$

This type of series can well overcome the singular integral problem in Eq. (3.3) and the Kutta boundary conditions of Eq. (2.12) at the plate trailing edge [8].

A substitution of Eq. (3.4) into Eq. (3.3) yields

$$\Theta_n(\xi) = \frac{1}{2\pi}\sum_{k=0}^{N_g} {}^{g}_{n}a_k \left[\int_{-1}^{1} \mathcal{G}_k(\xi')\mathcal{K}(\xi,\xi')\,d\xi'\right]. \tag{3.5}$$

Next, a numerical evaluation of the above equation at M uniformly discrete points within $[-1, 1]$ allows us the following equation

$${}^{g}_{n}\mathbf{C}_{M\times(N_g+1)} \cdot {}^{g}_{n}\mathbf{a}_{(N_g+1)\times 1} = {}^{\theta}_{n}\mathbf{q}_{M\times 1}, \tag{3.6}$$

where

$$\begin{aligned} {}^{g}_{n}\mathbf{a} &= [{}^{g}_{n}a_0, \ldots, {}^{g}_{n}a_{Ng}]^T, \\ {}^{\theta}_{n}\mathbf{q} &= [\Theta_n(\xi_1), \ldots, \Theta_n(\xi_M)]^T, \\ {}^{g}_{n}\mathbf{C}_{m,k+1} &= \frac{1}{2\pi}\int_{-1}^{1} \mathcal{G}_k(\xi')\mathcal{K}(\xi_m,\xi';\varsigma,\chi)\,d\xi', \\ \xi_m &= 2\frac{m-1}{M-1} - 1, \quad (1 \le m \le M). \end{aligned}$$

In Eq. (3.6), there are $N_g + 1$ unknown coefficients but M ($M \gg N_g$) equations. Thus Eq. (3.6) is an inconsistent equation, and its least squares solution is utilized; thus

$${}^{g}_{n}\mathbf{a} = \left({}^{g}_{n}\mathbf{C}^T \cdot {}^{g}_{n}\mathbf{C}\right)^{-1} \cdot {}^{g}_{n}\mathbf{C}^T \cdot {}^{\theta}_{n}\mathbf{q}, \tag{3.7}$$

and next we can substitute the above results into Eq. (3.4) for Υ_n first and then into Eq. (3.1b) for the solution of γ.

3.2. Least squares solution of instability equations

To solve Eq. (2.36), we start with considering Eq. (3.1) in Eq. (2.36a) and then arrive at

$$\sum_{n=1}^{N} A_n \left[\Theta_n(\xi) - \frac{\lambda}{16} \int_{-1}^{\xi} (\xi - s)^2 \Upsilon_n[\Theta_n](s)\, ds \right] = 1. \tag{3.8}$$

Note that the condition of Eq. (2.36b) has already been satisfied because of Eq. (3.2). We can first determine the coefficients of ${}^{g}_{n}a_k$ from Eq. (3.5) and substitute them into Eqs. (3.4) and then (3.8) into for A_n. Finally, Eq. (3.8) is also numerically evaluated at the same discrete points ξ_m (these discrete points have been also used for the solution of γ in Section 3.1), and then the following equations are obtained:

$$ {}^{\gamma}\mathbf{C}_{M\times N} \cdot \mathbf{A}_{N\times 1} = \mathbf{1}_{M\times 1}, \tag{3.9}$$

where

$$\mathbf{A} = [A_1, \ldots, A_N]^T,$$

$${}^{\gamma}\mathbf{C}_{m,n}(\lambda) = \Theta_n(\xi_m) - \frac{\lambda}{16} \int_{-1}^{\xi_m} (\xi_m - s)^2 \Upsilon_n[\Theta_n](s)\, ds.$$

The least squares solution of Eq. (3.9) is obtained as

$$\mathbf{A}(\lambda) = ({}^{\gamma}\mathbf{C}^T \cdot {}^{\gamma}\mathbf{C})^{-1} \cdot {}^{\gamma}\mathbf{C}^T, \tag{3.10}$$

and then a substitution of the above solution of $\mathbf{A}$ into Eq. (3.9) gives an error function in terms of λ; thus

$$e(\lambda) = \max |{}^{\gamma}\mathbf{C}(\lambda) \cdot \mathbf{A}(\lambda) - \mathbf{1}|. \tag{3.11}$$

Obviously, the error function varies as λ is varying; however, it will reach the minimum value when $\lambda \to \lambda_{\mathrm{cr}}$ (see [9, 40] for details); that is

$$\lim_{\lambda \to \lambda_{\mathrm{cr}}} e = \min[e(\lambda)]. \tag{3.12}$$

Let λ vary continuously and calculate the error function $e(\lambda)$ for every λ, and then we can find the critical value, λ_{cr}. Finally, we substitute λ_{cr} into Eq. (3.10) for $\mathbf{A}$ and then into Eq. (3.1a) for θ_{cr}.

4. Results and discussion

4.1. Convergence analysis

This section aims at the convergence of the current numerical approximated solution. First, we evaluate the solution of $\gamma(\xi)$ by specifying the plate slope $\theta(\xi)$ in Eq. (2.9) as the n-th natural mode of a free-clamped beam, i.e.,

$$\theta_n(\xi) = -\beta_n \sin\beta_n(1-\xi) - \beta_n \sinh\beta_n(1-\xi) + \frac{\sin 2\beta_n - \sinh 2\beta_n}{\cos 2\beta_n + \cosh 2\beta_n}[\beta_n \cos\beta_n(1-\xi) - \beta_n \cosh\beta_n(1-\xi)], \tag{4.1}$$

where β_n is the n-th root of the equation $\cos 2\beta_n \cosh 2\beta_n = -1$.

First, we aim at the accuracy of the calculation of the vortex distribution. Figures 6(a, b) shown that the induced velocity of the calculated vortex distribution on the plate is consistent with the down-wash of the plate ($v_I = \theta$) under the slope of θ_n ($n = 1, 2, 3$), which indicates the accuracy of the vortex distribution. It is also seen that the Glauert expansion with $N_g = 7$ is convergent for the present numerical solution of the vortex distribution.

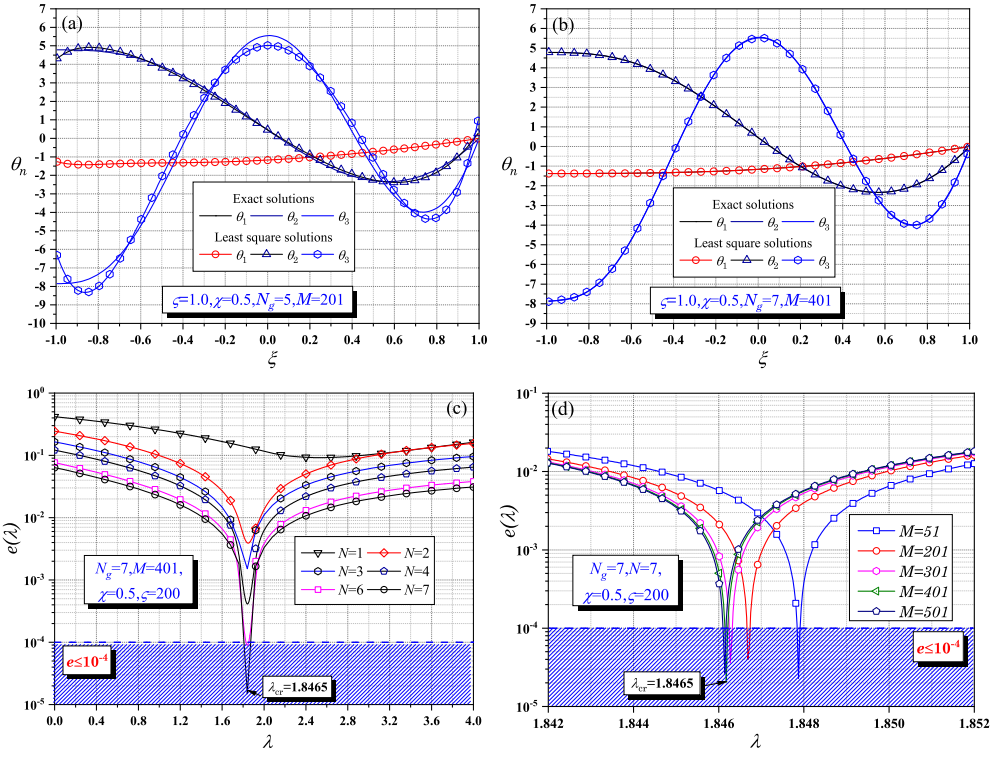

FIG. 6. Convergence analysis of the present approximated solution of instability equation.

Now, we move to the convergence analysis of the present approximated solution of instability equation. Firstly, we consider the case without the channel effect, i.e., $\varsigma \gg 1$, $\kappa = \chi\zeta\ (= d/L) \gg 1$, (in the present calculation we use $\varsigma = 200$, $\chi = 0.5$). This case has been studied in [29, 39, 40], and the critical dynamic pressure of this case is denoted as $\lambda_{\rm cr}^{\infty}$. Figure 6(c) shows that the error functions for various N have similar change laws with λ varying, and they reach their minimum values almost at the same dynamic pressure, i.e., $\lambda_{\rm cr}^{\infty}$. The results of Fig. 6(c) suggest using $N = 7$ for $e < 10^{-4}$ for the present calculation, and the error function in terms of M for $N = 7$ is evaluated in Fig. 6(d). It is seen that there is a significant decrease of the error near some dynamic pressure, and the minimum error also suggests $\lambda_{\rm cr}^{\infty}$. With less than 10^{-4} error, it is suggested $M = 401$ for the present numerical solution. As shown in Figs. 6(a, b), $\lambda_{\rm cr}^{\infty}$ decreases gradually and finally converges to $\lambda_{\rm cr}^{\infty} = 1.846$ as N or M increasing, which agrees well with [29] ($\lambda_{\rm cr}^{\infty} = 1.848$), [39] ($\lambda_{\rm cr}^{\infty} = 1.850$) and [40] ($\lambda_{\rm cr}^{\infty} = 1.843$) listed in Table 1.

When the distance between the plate and channel upper wall is considerable, i.e., $\varsigma \gg 1$, $\varsigma - \kappa \geq 1$, the present problem becomes the case with a unilateral

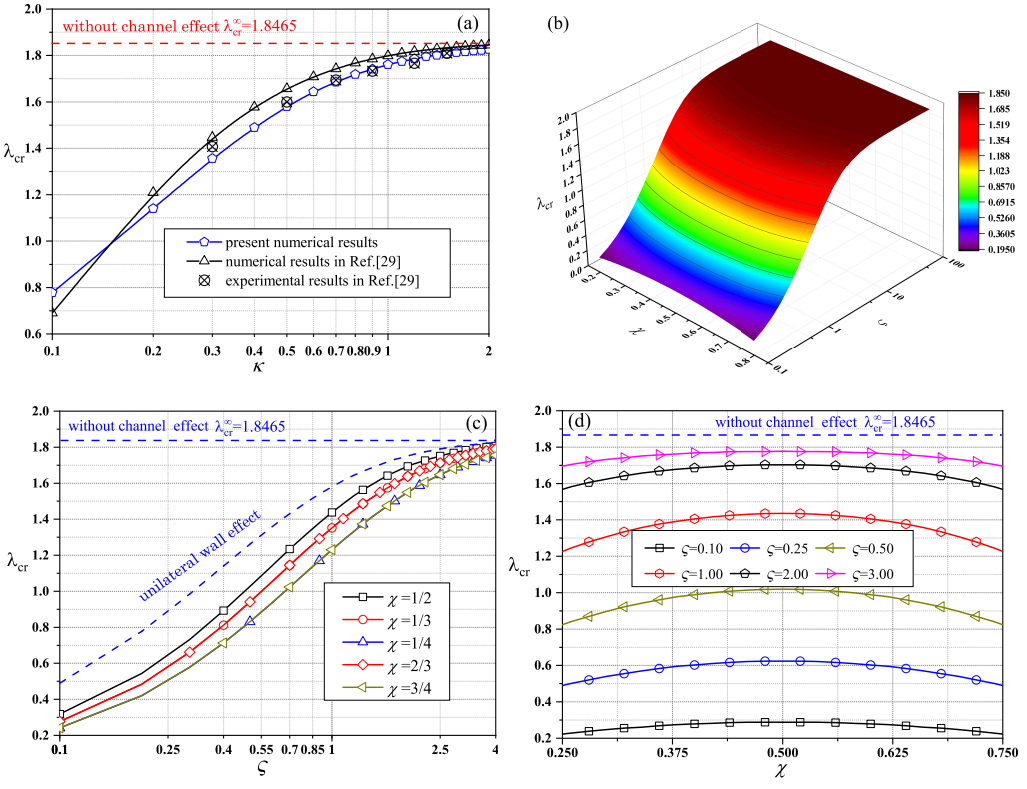

FIG. 7. Results of the instability boundaries.

Table 1. Comparison of λ_{cr}^{∞} between the present study and others.

References	Research type	
	Numerical	Experimental
Zhang *et al.* [29]	1.848	1.816
Sader *et al.* [39]	1.850	2.420
Serry and Tuffaha [40]	1.843	–
Present study	1.846	–

wall effect, which has been studied numerically and experimentally in [29]. For comparison with this study, we set $\varsigma = 200$ and let κ vary from $\kappa = 0.1$ to 2.0. The instability boundary λ_{cr} of the present study and [29] are compared and shown in Fig. 7(a). With the increase of κ, λ_{cr} finally approaches its limit $\lambda_{cr}^{\infty} = 1.8465$ and it becomes the case of unbounded flow. The above comparative study fully shows the feasibility and accuracy of the present approximated solution of the present instability problem.

4.2. Instability behaviors

Now we move to study the effect of characteristic parameters of the channel (ς, χ) on the plate instability behaviors. The instability boundary of λ_{cr} in terms of ς and χ is plotted in Fig. 7(b). In Fig. 7(c), the instability curves are plotted in terms of ζ for various χ. It is seen that they show similar exponential growth as ς increases and finally tend to $\lambda_{cr}^{\infty} = 1.8465$. Figure 7(d) plots the instability curves in terms of χ for various ς. Similar parabolic variations and the symmetry about $\chi = \frac{1}{2}$ are clearly observed in this figure. From Fig. 7, it is seen that the channel confinement plays a significant destabilizing effect on the plate. The critical dynamic pressure decreases significantly as the channel confinement increases (decrease of ς). When $\chi \neq \frac{1}{2}$, i.e., the plate is not in the middle of the channel, λ_{cr} is always smaller than the case with a unilateral wall effect, and the closer the plate is to one of the walls, the lower λ_{cr} is.

The results of plate pressure in critical states (namely, p_{cr}) are plotted in Figs. 8(a, c). It is seen that p_{cr} under different cases are almost not dependent on the characteristic parameters of the channel. The pressure always has a maximum at the plate leading edge; however, it decays rapidly and becomes zero at the plate trailing edge, implying that the Kutta condition of Eq. (2.6d) has been well satisfied at the end edge. The vortex sheet strength in critical states (γ_{cr}) is shown in Figs. 8(b, d). Compared with p_{cr}, γ_{cr} is very sensitive to these two parameters, and interestingly, they show obvious similarity.

The plate instability modes, i.e., the critical plate slopes (θ_{cr}), for various ζ and χ, are shown in Fig. 9. For comparison, the normalized first-order natural

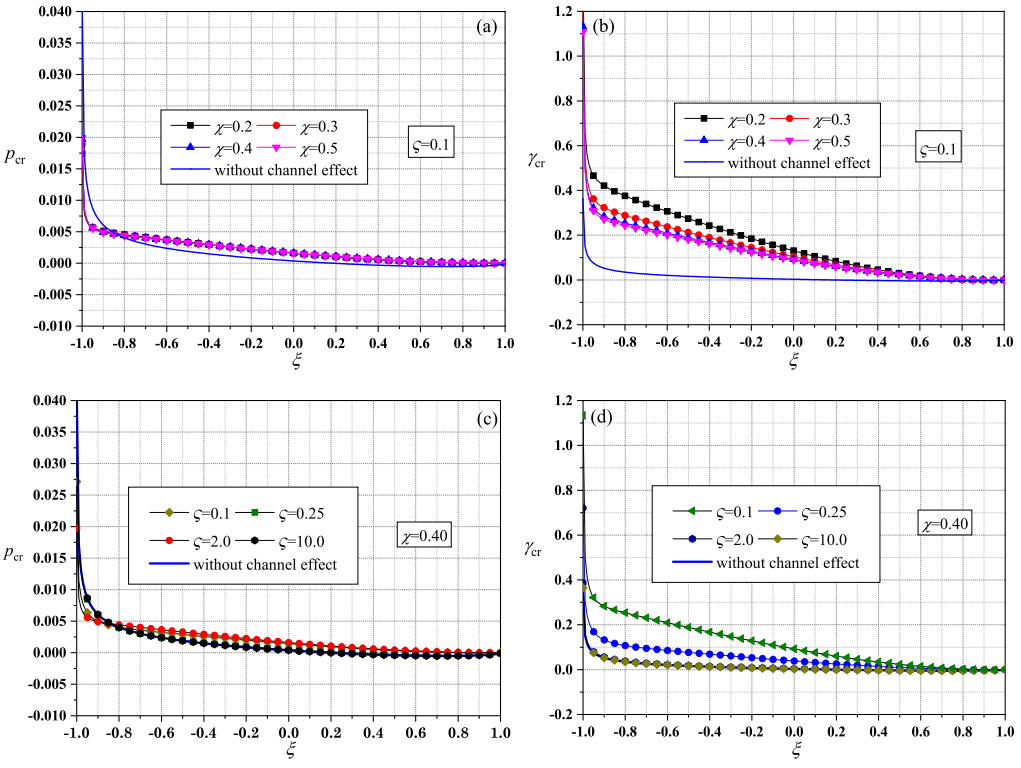

FIG. 8. Results of (a, c) the critical pressure distribution $p_{\rm cr}$ and (b, d) the critical vortex sheet strength $\gamma_{\rm cr}$.

mode of the plate, i.e., θ_1 given in Eq. (4.1), is also plotted in this figure by solid blue lines. It is seen that these critical slope curves have no significant difference from the natural ones, implying that the plate's first-order nature mode mainly dominates its instability mode.

The similarity of instability modes and the critical pressure further motivates us to explore their variation mechanics on parameters. We design to begin our analysis with a revisit to Eq. (2.36a), after differentiating this equation to ξ, we arrive at

$$\theta_{\rm cr}^{(1)}(\xi;\varsigma,\chi) = -{}^{\rm a}\mathcal{M}_{\rm cr}[\theta_{\rm cr}](\xi;\varsigma,\chi), \tag{4.2}$$

where the operator ${}^{\rm a}\mathcal{M}_{\rm cr}$ is defined as

$${}^{\rm a}\mathcal{M}_{\rm cr}(\xi;\varsigma,\chi) = \int_{-1}^{\xi} (\xi - s) p_{\rm cr}(s;\varsigma,\chi)\, ds,$$

and it is called aero-moment. And $p_{\rm cr}$ is called the aero-pressure.

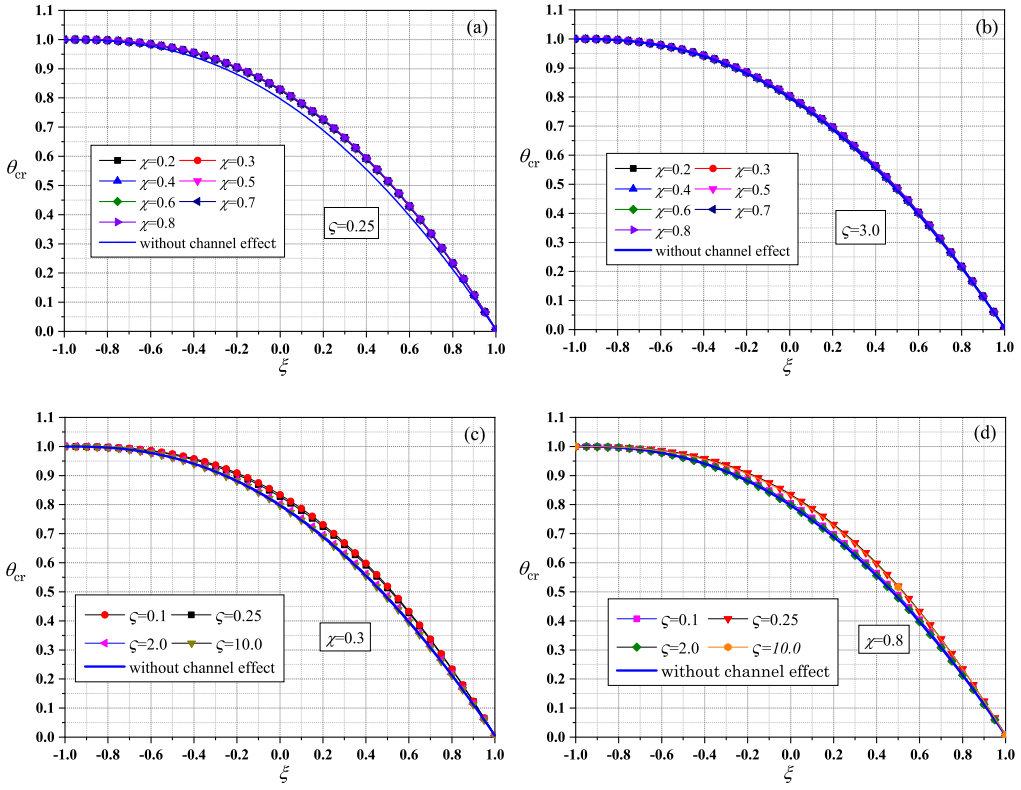

FIG. 9. Results of the plate instability modes (the critical plate slope $\theta_{\rm cr}$).

The results of ${}^{\rm a}\mathcal{M}_{\rm cr}$ are shown in Figs. 10(a, c). It is seen that they have similar changing rule and are not sensitive to the characteristic parameters of the channel. To find the relationship between ${}^{\rm a}\mathcal{M}_{\rm cr}$ and $\theta_{\rm cr}$, we integrate Eq. (4.2) along the plate and consider Eq. (2.33), thus we obtain

$$\theta_{\rm cr}(-1;\varsigma,\chi) = \int_{-1}^{1} {}^{\rm a}\mathcal{M}_{\rm cr}(s;\varsigma,\chi)\,ds \equiv 1. \tag{4.3}$$

This equation demonstrates that the total moment of aero-pressure in a critical state is also independent of ζ and χ, and always remains constant at 1. It also, in turn, implies that the critical bending moment in the plate is also invariant and independent of characteristic parameters of the channel. It may explain why the plate instability slopes are similar and close to the natural modes that are irrelevant to the channel, as seen in Fig. 9.

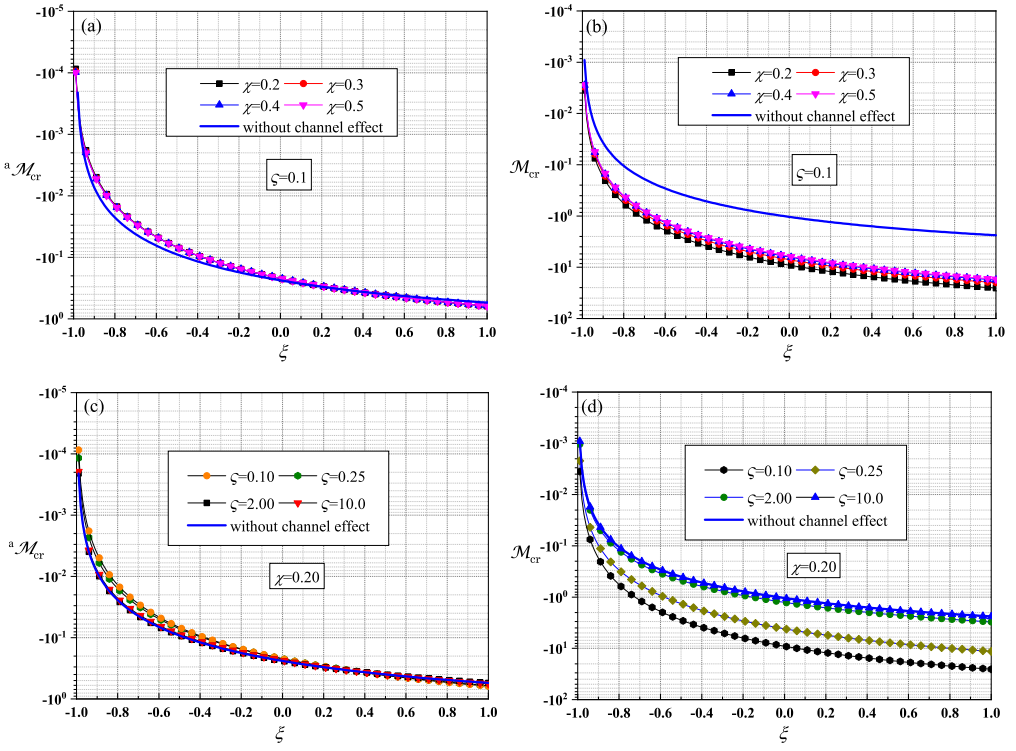

FIG. 10. Results of (a, c) the critical aero-moment ${}^{\mathrm{a}}\mathcal{M}_{\mathrm{cr}}$ and (b,d) the critical aero-moment coefficients $\mathcal{M}_{\mathrm{cr}}$.

Next, we further consider Eq. (2.11) in Eq. (4.3) and then obtain

$$-\frac{\lambda_{\mathrm{cr}}}{8}\int_{-1}^{1}\mathcal{M}_{\mathrm{cr}}(s;\varsigma,\chi)\,ds\equiv 1, \tag{4.4}$$

where

$$\mathcal{M}_{\mathrm{cr}}(\xi;\zeta,\chi)=\int_{-1}^{\xi}(\xi-s)\gamma_{\mathrm{cr}}(s;\zeta,\chi)\,ds,$$

is related to the moment called as the aero-moment coefficient. The results of $\mathcal{M}_{\mathrm{cr}}$ are shown in Figs. 10(b, d), and it is seen that $\mathcal{M}_{\mathrm{cr}}$, as expected, is quite sensitive to the characteristic parameters of the channel.

Equation (4.4) clearly gives the dependence between λ_{cr} and γ_{cr}, and they are closely related to ζ and χ. Most importantly, this relation allows us the following scaling relation

$$\log\lambda_{\mathrm{cr}}(\varsigma,\chi)\propto -1\cdot\log\mathcal{L}_{\mathrm{cr}}(\varsigma,\chi), \tag{4.5}$$

where

$$\mathcal{L}_{\rm cr}(\varsigma,\chi)=\int\limits_{-1}^{1}\mathcal{M}_{\rm cr}(s;\varsigma,\chi)\,ds.$$

The numerical results of $\mathcal{L}_{\rm cr}^{-1}(\varsigma,\chi)$ are shown in Fig. 11, and the scaling results of Eq. (4.5) in Fig. 12. It is seen that the present numerical solutions agree with the theoretical scaling rule well. This formulation can be applied to evaluate the varying rule of the instability boundary and to predict it.

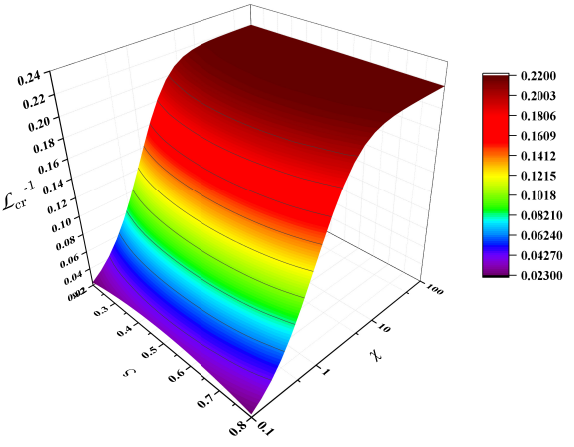

FIG. 11. Numerical evaluation of the function $\mathcal{L}_{\rm cr}^{-1}(\zeta,\chi)$.

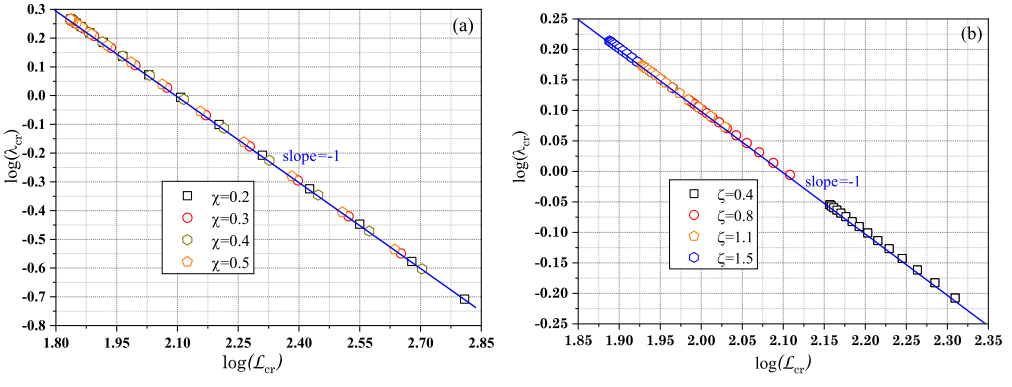

FIG. 12. Numerical results of scaling analysis.

Interestingly, Eq. (4.4) also allows us to establish the following relation between the cases whether the channel effect is considered or not; thus

$$\lambda_{\mathrm{cr}}\mathcal{L}_{\mathrm{cr}}(\varsigma,\chi)=\lambda_{\mathrm{cr}}^{\infty}\mathcal{L}_{\mathrm{cr}}(\infty,0.5), \tag{4.6}$$

and

$$\lambda_{\mathrm{cr}}(\zeta,\chi)=\frac{\mathcal{L}_{\mathrm{cr}}(\infty,0.5)}{\mathcal{L}_{\mathrm{cr}}(\varsigma,\chi)}\lambda_{\mathrm{cr}}^{\infty}. \tag{4.7}$$

The above equation gives a semi-analytic approximation of the instability boundary. An analytical expression of the function $\mathcal{L}_{\mathrm{cr}}^{-1}(\varsigma,\chi)$ is not available currently, and it is still underway and will be reported elsewhere.

5. Summary

This paper studies the instability of an inverted cantilevered plate in a channel flow. It gains motivation from the authors' previous work and aims to reveal the underlying mechanics of such a problem and the channel's effect. The present modeling procedure emphasizes the approximation of the solution rather than the equations. Unlike other studies based on the eigenvalue calculation of approximated system equations, this study presents a theoretical modeling procedure in a continuum sense without equation-level approximation. It represents this instability problem in the state space and as a function approximation problem with the critical flow speed and instability mode as the objective functions in mathematics. It also develops a convergent numerical strategy for approximating the solution with the help of series expansion and the least squares method.

Numerical results show Glauert's series can solve Kutta's condition at the plate trailing edge. The present theoretical model and its numerical solutions can successfully predict the instability behavior of such an aeroelastic instability problem and the channel's effect. The channel destabilizes the plate and efficiently decreases its critical speed. This result has also been found by [10] in the models they examined, which included the clamped-clamped, clamped-pinned, and pinned-pinned boundary conditions. Asymmetric plate placements have a more significant effect than symmetric ones.

Compared with the case of a unilateral wall, the channel effect on the plate instability is more significant, indicating that using the channel confinements and plate placements can give the plate a broader and more diverse variation range in the critical speed. It can be utilized to improve the high-speed train skin design [7–9], heat enhancement [30], energy harvesting technologies [36, 37], and also to provide insights into physical phenomena [31, 32] that rely on such a plate model. This paper provides an analysis framework, including the theoretical modeling strategy in a continuum sense and the numerical solution approximation method, that could apply to other similar problems in the future.

It is essential to point out that this paper applies the least squares method to approximate the solutions of the instability equation, which is essentially a math-

ematical optimization method. Applying other optimization algorithms to this problem may develop different numerical approaches, which is an open problem for interested readers.

Acknowledgements

This work is supported by the National Natural Science Foundation of China (Grant Nos: 12072298; 12172311).

Conflict of interest

The authors declare that they have no conflict of interest.

References

1. E.H. Dowell, *Aeroelasticity of Plates and Shells*, Noordhoff International Publishing, Leyden, 1975.
2. M.J. Shelley, J. Zhang, *Flapping and bending bodies interacting with fluid flows*, Annual Review of Fluid Mechanics, **43**, 449–465, 2011, doi: 10.1146/annurev-fluid-121108-145456.
3. E.H. Dowell, *Nonlinear oscillations of a fluttering plate II*, AIAA Journal, **5**, 1856–1862, 1967, doi: 10.2514/6.1967-13.
4. S.D. Algazin, I.A. Kijko, *Aeroelastic Vibrations and Stability of Plates and Shells*, De Gruyter Studies in Mathematical Physics, **25**, 2014, doi: 10.1515/9783110338379.20.
5. P. Li, Y.R. Yang, W. Xu, *Nonlinear dynamics analysis of a two-dimensional thin panel with an external forcing in incompressible subsonic flow*, Nonlinear Dynamics, **67**, 251–267, 2012, doi: 10.1007/s11071-011-0162-8.
6. P. Li, D.C. Zhang, Z.W. Li, C. Dai, Y. Yang, *Bifurcations and post-critical behaviors of a nonlinear curved plate in subsonic airflow,* Archive of Applied Mechanics, **89**, 2, 343–362, 2019, doi: 10.1007/s00419-018-1471-x.
7. P. Li, Z.W. Li, S. Liu, Y. Yang, *Non-linear limit cycle flutter of a plate with Hertzian contact in axial flow,* Journal of Fluids and Structures, **81**, 131–160, 2018, doi: 10.1016/j.jfluidstructs.2018.04.014.
8. P. Li, Z.W. Li, C.D. Dai, Y. Yang, *On the non-linear dynmaics of a forced plate with boundary conditions correction in subsonic flow,* Applied Mathematical Modelling, **64**, 15–46, 2018, doi: 10.1016/j.apm.2018.07.012.
9. D.C. Zhang, P. Li, Y.Z. Zhu, Y. Yang, *Aeroelastic instability of an inverted cantilevered plate with cracks in axial subsonic airflow*, Applied Mathematical Modelling, **107**, 782–801, 2022, doi: 10.1016/j.apm.2022.03.019.
10. C.Q. Guo, M.P. Païdoussis, *Stability of rectangular plates with free side-edges in two-dimensional inviscid channel flow*, Journal of Applied Mechanics, **67**, 1, 171–176, 2000, doi: 10.1115/1.321143.

11. K. SHELE, R. MITTAL, *Flutter instability of a thin flexible plate in a channel*, Journal of Fluid Mechanics, **786**, 39–46, 2016, doi: 10.1017/jfm.2015.632.

12. Y. WATANABE, S. SUZUKI, M. SUGIHARA, Y. SUEOKA, *An experimental study of paper flutter*, Journal of Fluids and Structures, **16**, 529–542, 2002, doi: 10.1006/jfls.2001.0435.

13. Y. WATANABE, K. ISOGAI, S. SUZUKI, M. SUGIHARA, *A theoretical study of paper flutter*, Journal of Fluids and Structures, **16**, 543–560, 2002, doi: 10.1006/jfls.2001.0436.

14. O. DOARE, S. MICHELIN, *Piezoelectric coupling in energy-harvesting fluttering flexible plates: linear stability analysis and conversion efficiency*, Journal of Fluids and Structures, **27**, (8), 1357–1375, 2011, doi: 10.1016/j.jfluidstructs.2011.04.008.

15. D.M. TANG, E.H. DOWELL, *Aeroelastic response and energy harvesting from a cantilevered piezoelectric laminated plate*, Journal of Fluids and Structures, **45**, 124–137, 2014, doi: 10.1016/j.jfluidstructs.2017.09.007.

16. M. CHEN, L.B. JIA, Y.F. WU, X.Z. YIN, Y.B. MA, *Bifurcation and chaos of a flag in an inviscid flow* , Journal of Fluids and Structures, **76**, 14–36, 2018, doi: 10.1016/j.jfluidstructs.2013.11.020.

17. A.D. LUCEY, *The excitation of waves on a flexible panel in a uniform flow*, Philosophical Transactions of the Royal Society A, **356**, 2999–3039, 1998, doi: 10.1098/rsta.1998.0306.

18. R. DE BREUKER, M.M. ABDALLA, Z. GÜRDAL, *Flutter of partially rigid cantilevered plates in axial flow*, AIAA Journal, **46**, 936–946, 2008, doi: 10.2514/1.31887.

19. J. ZHANG, N.S. LIU, X.Y. LU, *Locomotion of a passively flapping flat plate*, Journal of Fluid Mechanics, **659**, 43–68, 2010, doi: 10.1017/S0022112010002387.

20. Y. YU, Y. LIU, X. AMANDOLESE, *A review on fluid-induced flag vibrations*, Applied Mechanics Reviews, **71**, 1, 010801, 2019, doi: 10.1115/1.4042446.

21. L. HUANG, *Flutter of cantilevered plates in axial flow*, Journal of Fluids and Structures, **9**, 2, 127–147, 1995, doi: 10.1006/jfls.1995.1007.

22. J. DUGUNDJI, E.H. DOWELL, B. PERKIN, *Subsonic flutter of panels on continuous elastic foundations*, AIAA Journal, **5**, 1146–1154, 1963, doi: 10.2514/3.1738.

23. A. KORNECKI, E.H. DOWELL, J. O'BRIEN, *On the aeroelastic instability of two-dimensional panels in uniform incompressible flow*, Journal of Sound and Vibration, **47**, 2, 163–178, 1976, doi: 10.1016/0022-460X(76)90715-X.

24. C. ELOY, C. SOUILLIEZ, L. SCHOUVEILER, *Flutter of a rectangular plate*, Journal of Fluids and Structures, **23**, 6, 904–919, 2007, doi: 10.1016/j.jfluidstructs.2007.02.002.

25. R.M. HOWELL, A.D. LUCEY, *Flutter of spring-mounted flexible plates in uniform flow*, Journal of Fluids and Structures, **59**, 370–393, 2015, doi: 10.1016/j.jfluidstructs.2015.09.009.

26. B.S.H. CONNELL, D.K.P. YUE, *Flapping dynamics of a flag in a uniform stream*, Journal of Fluids and Structures, **581**, 33–67, 2007, doi: 10.1017/S0022112007005307.

27. L. ZHU, C.S. PESKIN, *Simulation of a flapping flexible filament in a flowing soap film by the immersed boundary method*, Journal of Computational Physics, **179**, 452–468, 2002, doi: 10.1006/jcph.2002.7066.

28. W.X. HUANG, S.J. SHIN, H.J. SUN, *Simulation of flexible filaments in a uniform flow by the immersed boundary method*, Journal of Computational Physics, **226**, 2206–2228, 2007, doi: 10.1016/j.jcp.2007.07.002.

29. D.C. Zhang, S. Liang, P. Li, Y. Yang, *A numerical and experimental study on the divergence instability of an inverted cantilevered plate in wall effect*, Archive of Applied Mechanics, **90**, 1509–1528, 2020, doi: 10.1007/s00419-020-01681-8.

30. S.G. Park, B. Kim, C.B. Chang, J. Ryu, H.J. Sung, *Enhancement of heat transfer by a self-oscillating inverted flag in a Poiseuille channel flow*, International Journal of Heat and Mass Transfer, **96**, 362–370, 2016, doi: 10.1016/j.ijheatmasstransfer.2016.01.043.

31. B. Fan, *Fluid-structure interactions of inverted leaves and flags*, Doctoral Dissertation, California Institute of Technology, 2015.

32. P. Buchak, C. Eloy, P.M. Reis, *The clapping book: wind-driven oscillations in a stack of elastic sheets*, Physical Review Letters, **105**, 19, 194301, 2010, doi: 10.1103/PhysRevLett.105.194301.

33. S. Michelin, O. Doaré, *Energy harvesting efficiency of piezoelectric flags in axial flows*, Journal of Fluid Mechanics, **714**, 489–504, 2013, doi: 10.1017/jfm.2012.494.

34. S.J. Simitses, D.H. Hodges, *Fundamentals of Structural Stability*, Elsevier Inc., 2006.

35. M. Tavallaeinejad, M.P. Païdoussis, M. Legrand, *Nonlinear static response of low-aspect-ratio inverted flags subjected to a steady flow*, Journal of Fluids and Structures, **83**, 413–428, 2018, doi: 10.1016/j.jfluidstructs.2018.09.003.

36. O. Ojo, K. Shoele, *Piezoelectric energy harvesting of an inverted flag behind a bluff body*, 73rd Annual Meeting of the APS Division of Fluid Dynamics, Chicago, Bulletin of the American Physical Society, **65**, 13, 2020.

37. S. Mazharmanesh, J. Young, F.B. Tian, J.C.S. Lai, *Energy harvesting of two inverted piezoelectric flags in tandem, side-by-side and staggered arrangements*, International Journal of Heat and Fluid Flow, **83**, 108589, 2020, doi: 10.1016/j.ijheatfluidflow.2020.108589.

38. M. Tavallaeinejad, M.P. Païdoussis, M. Legrand, M. Kheri, *Instability and the post-critical behaviour of two-dimensional inverted flags in axial flow*, Journal of Fluid Mechanics, **890A**, 14, 1–14, 2020, doi: 10.1017/jfm.2020.111.

39. J.E. Sader, J. Cossé, D. Kim, B. Fan, *Large-amplitude flapping of an inverted flag in a uniform steady flow-a vortex-induced vibration*, Journal of Fluid Mechanics, **793**, 524–555, 2016, doi: 10.1017/jfm.2016.139.

40. M. Serry, A. Tuffaha, *Static stability analysis of a thin plate with a fixed trailing edge in axial subsonic flow: Possio integral equation approach*, Applied Mathematical Modelling, **63**, 644–659, 2018, doi: 10.1016/j.apm.2018.07.005.

41. D. Kim, J. Cossé, C.H. Cerdeira, M. Gharib, *Flapping dynamics of an inverted flag*, Journal of Fluid Mechanics, **736R1**, 1–12, 2013, doi: 10.1017/jfm.2013.555.

42. A. Goza, T. Colonius, J.E. Sader, *Global modes and nonlinear analysis of inverted-flag flapping*, Journal of Fluid Mechanics, **857**, 312–344, 2016, doi: 10.1017/jfm.2018.728.

43. P.S. Gurugubelli, R.K. Jaiman, *Self-induced flapping dynamics of a flexible inverted foil in a uniform flow*, Journal of Fluid Mechanics, **781**, 657–694, 2015, doi: 10.1017/jfm.2015.515.

44. J. Ryu, S.G. Park, B. Kim, H.J. Sung, *Flapping dynamics of an inverted flag in a uniform flow*, Journal of Fluids and Structures, **57**, 159–169, 2015, doi: 10.1016/j.jfluidstructs.2015.06.006.

45. J.W. PARK, J. RYU, H.J. SUNG, *Effects of the shape of an inverted flag on its flapping dynamics*, Physics of Fluids, **31**, 2, 021904, 2019, doi: 10.1017/jfm.2013.555.

46. C. TANG, N.S. LIU, X.Y. LU, *Dynamics of an inverted flexible plate in a uniform flow*, Physics of Fluids, 27, 7, 073601, 2015, doi: 10.1063/1.4923281.

47. K. SHOELE, R. MITTAL, *Energy harvesting by flow-induced flutter in a simple model of an inverted piezoelectric flag*, Journal of Fluid Mechanics, **790**, 582–606, 2016, doi: 10.1017/jfm.2016.40.

48. A.V. BALAKRISHNAN, *Aeroelasticity: The Continuum Theory*, Springer Science and Business Media, 2012.

Received April 15, 2023; revised version December 14, 2023.
Published online January 29, 2024.